

RESEARCH ARTICLE

SPECIAL ISSUE: RECONSTITUTING CELL BIOLOGY

Activation of mammalian cytoplasmic dynein in multimotor motility assays

Gina A. Monzon^{1,*}, Lara Scharrel^{2,*}, Ludger Santen^{1,‡} and Stefan Diez^{2,3,‡}

ABSTRACT

Long-range intracellular transport is facilitated by motor proteins, such as kinesin-1 and cytoplasmic dynein, moving along microtubules (MTs). These motors often work in teams for the transport of various intracellular cargos. Although transport by multiple kinesin-1 motors has been studied extensively in the past, collective effects of cytoplasmic dynein are less well understood. On the level of single molecules, mammalian cytoplasmic dynein is not active in the absence of dynactin and adaptor proteins. However, when assembled into a team bound to the same cargo, processive motility has been observed. The underlying mechanism of this activation is not known. Here, we found that in MT gliding motility assays the gliding velocity increased with dynein surface density and MT length. Developing a mathematical model based on single-molecule parameters, we were able to simulate the observed behavior. Integral to our model is the usage of an activation term, which describes a mechanical activation of individual dynein motors when being stretched by other motors. We hypothesize that this activation is similar to the activation of single dynein motors by dynactin and adaptor proteins.

This article has an associated First Person interview with the first author of the paper.

KEY WORDS: Mammalian cytoplasmic dynein, Gliding motility assay, Stochastic modeling

INTRODUCTION

Motor proteins such as kinesin and dynein are relevant for a multitude of cellular functions. One of them is intracellular cargo transport, which is often performed by the collective action of small groups of motors. The collective effects of multiple kinesin-1 motors working together have been studied extensively in the past, both experimentally and theoretically (Bieling et al., 2010; Klein et al., 2014a,b; Pan et al., 2006; Scharrel et al., 2014; Larson et al., 2009), whereas the collective effects of dynein motors have so far been studied for axonemal dynein, and yeast and mammalian cytoplasmic dynein (Sakakibara et al., 1999; Shimizu et al., 2014; Derr et al., 2012). For mammalian cytoplasmic dynein (herein referred to as dynein), high processivity and increased transport velocities have been observed for teams of multiple dynein motors.

Examples include bead assays with dynactin and adaptor proteins (McKenney et al., 2014), bead assays with a large cargo but without adaptor proteins (Belyy et al., 2016), and DNA-origami assays without adaptor proteins but with multiple dynein motors (Torisawa et al., 2014). Furthermore, previous studies reported high microtubule (MT) gliding velocities on surfaces coated with multiple dynein motors (MT gliding assays) (Torisawa et al., 2014; Nicholas et al., 2015; Tanenbaum et al., 2013). In contrast, mainly diffusive motility was observed when cargo was coupled to individual, single dynein motors (Torisawa et al., 2014; Belyy et al., 2016). In fact, individual, single dynein motors only became processive in the presence of dynactin and adaptor proteins, such as BicD proteins (McKenney et al., 2014; Schlager et al., 2014). These findings indicate that activation of dynein is necessary for directed motility and that cargo binding alone does not lead to this activation. Upon closer review of previous studies on the activation itself, we find that in the case of activation by adaptor proteins, the two dynein motor domains are separated and parallelly aligned in the processive state, whereas in the auto-inhibited state they are stacked together (Zhang et al., 2017). Similar observations were reported by Torisawa et al. (2014), but without adaptor proteins: They showed that in the auto-inhibited state, the two motor heads are stacked together, but when they physically separated them unidirectional and processive motility were observed. These observations led to the assumption that the dynein motors can be activated mechanically by motor stretching. In this study, we present a combined experimental and theoretical approach to study collective effects in transport by multiple dynein motors. In particular, we investigate the transport velocity of MTs gliding on dynein-functionalized surfaces as a function of motor density and MT length. We describe our experimental data by a mathematical model based on single-molecule parameters, which includes the mechanical activation of individual dynein motors.

RESULTS

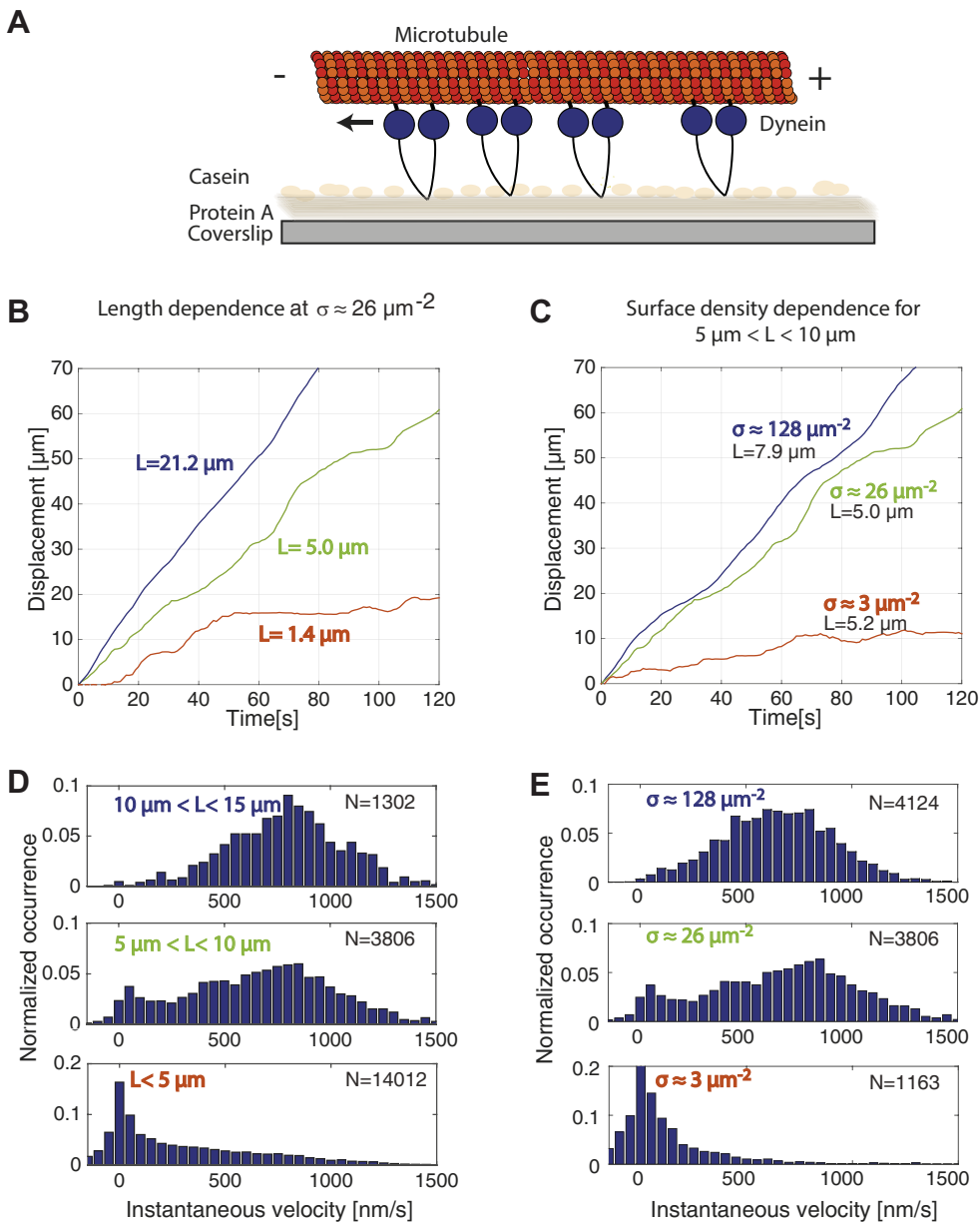
Experiments

We performed *in vitro* MT gliding motility assays on surfaces coated with dynein (Fig. 1A). At a dynein surface density of $\sim 26 \mu\text{m}^{-2}$, we found that long MTs ($L_{MT} > 10 \mu\text{m}$) primarily moved with constant and fast velocities (Fig. 1B). Short MTs ($L_{MT} < 5 \mu\text{m}$) moved with slow velocities close to zero or only showed diffusive behavior along their long axis, and MTs of intermediate length ($5 \mu\text{m} < L_{MT} < 10 \mu\text{m}$) moved with phases of fast and slow velocity, often resulting in a stop-and-go-like behavior. We then investigated the gliding velocity as a function of dynein surface density (experimentally varied by incubating the surface with solutions containing different dynein concentrations) at constant MT length ($5 \mu\text{m} < L_{MT} < 10 \mu\text{m}$, Fig. 1C). At high dynein surface density ($128 \mu\text{m}^{-2}$), we observed that MTs moved primarily with constant and fast velocities. At low dynein surface density ($3 \mu\text{m}^{-2}$), MTs moved with low velocities close to zero. At intermediate surface

¹Center for Biophysics, Department of Physics, Saarland University, D-66123, Saarbrücken, Germany. ²B CUBE Center for Molecular Bioengineering, Technische Universität Dresden, D-01307 Dresden, Germany. ³Max Planck Institute of Molecular Cell Biology and Genetics, D-01307 Dresden, Germany. *These authors contributed equally to this work

‡Authors for correspondence (l.santen@mx.uni-saarland.de; stefan.diez@tu-dresden.de)

© L.S., 0000-0001-8478-9667; S.D., 0000-0002-0750-8515

**Fig. 1. Experimental setup.**

(A) Schematic diagram of the gliding motility assay. Dynein (recombinant cytoplasmic human dynein) was bound to the surface of a flow cell unspecifically using protein A. The surface was blocked by casein to prevent unspecific attachment of proteins. Gliding of the fluorescently labeled MTs was observed by fluorescence microscopy. (B) Time-distance plots of individual gliding MTs of three lengths at intermediate dynein surface density ($26 \mu\text{m}^{-2}$). (C) Time-distance plot of individual gliding MTs of intermediate length ($5 \mu\text{m} < L_{MT} < 10 \mu\text{m}$) at three dynein surface densities. (D) Normalized histograms of the instantaneous velocity for many gliding MTs (with number of data points) of three length scales at fixed dynein surface density ($26 \mu\text{m}^{-2}$). (E) Normalized histograms of instantaneous velocity for many gliding MTs (with number of data points) of fixed length ($5 \mu\text{m} < L_{MT} < 10 \mu\text{m}$) at three dynein surface densities.

density ($26 \mu\text{m}^{-2}$), MTs moved with phases of fast and slow velocity, often resulting in a stop-and-go-like behavior. Taken together, these results suggest that dynein motility depends predominantly on the number of dynein motors interacting with the MTs. To quantify our observations, we plotted histograms of the instantaneous gliding velocity (i.e. the velocities derived from the distances that individual MTs moved between two consecutive frames divided by the elapsed time, Fig. 1D,E). At intermediate dynein surface density ($26 \mu\text{m}^{-2}$, Fig. 1D), we observed: (1) a unimodal velocity distribution with a peak at ~ 800 nm/s for long MTs ($L_{MT} > 10 \mu\text{m}$); (2) a bimodal velocity distribution with one peak around zero velocity and another peak around 800 nm/s for MTs of intermediate length ($5 \mu\text{m} < L_{MT} < 10 \mu\text{m}$); and (3) a unimodal-like velocity distribution exhibiting a peak around zero velocity and a tail towards higher velocities for short MTs ($L_{MT} < 5 \mu\text{m}$). Similar velocity histograms were observed for MTs of fixed length ($5 \mu\text{m} < L_{MT} < 10 \mu\text{m}$) and different surface densities (Fig. 1E): (1) a unimodal velocity distribution with a peak at ~ 750 nm/s for a high dynein surface density ($128 \mu\text{m}^{-2}$); (2) a

bimodal velocity distribution with one peak around zero velocity and another peak at ~ 800 nm/s for an intermediate dynein surface density ($26 \mu\text{m}^{-2}$); and (3) a unimodal-like velocity distribution exhibiting a peak around zero velocity and a tail towards higher velocities for a low dynein surface density ($3 \mu\text{m}^{-2}$). These results reinforce the notion that uniform and fast MT gliding is only observed when a sufficiently large number of dynein motors is available for MT transport. We hypothesize that the improved motility at high motor density and/or for long MTs is a cooperative effect of multiple dynein motors working together.

Model

We introduce a mathematical model including force-dependent stepping and detachment rates as well as a mechanical activation of the individual dynein motors. The mathematical model is based on the model described in Klein et al. (2014a), which has already been successfully applied to kinesin-based transport (see also Materials and Methods and the Supplementary Information for the kinesin-based MT gliding assay). Here, the modeling approach

was adapted to the geometry of the MT gliding assay, and the motor behavior and parameters were adjusted to the dynein properties, where experimental data were available (see Table S1 for details on references of the model parameter). For the MT gliding assay, we describe the MTs as rigid one-dimensional objects, which can move back and forward at constant height above the planar surface coated randomly with dynein motor proteins (Fig. 2A). The dynein motors are modeled as linear springs, which are permanently attached to the surface at positions x_c^i (position of the motor tail on the surface) in the stationary coordinate system of the surface (herein referred to as surface system). The dynein motor heads can either be unbound from the MT (detached motor) or bound to the MT (attached motor). An attached motor exerts a force on the MT, which is proportional to its stretching $\Delta x_i = x_j^i(t) + X_{MT}(t) - x_c^i$, where $X_{MT}(t)$ denotes the MT minus end position in the surface system and $x_j^i(t)$ denotes the

position of the motor head on the MT in the moving coordinate system of the MT with origin at the MT minus end [herein referred to as MT system, $x_j^i(t)$ ranging from zero (MT minus end) to the MT length L_{MT} (MT plus end)]. Several attached motors are mechanically coupled via the rigid MT, i.e. they mutually apply forces on each other. If all dynein motors together induce a net force to the MT, the MT (plus the motor heads that are attached to the MT in the MT system) is moved to the equilibrium position, where the forces from all motors attached to the MT are balanced. This implementation of the MT motility is in agreement with the solution of the Langevin equation, i.e. that after a motor event the MT always reaches its equilibrium position (considering the kinetic rates of our mathematical model and the experimentally given viscosity) before the next motor event occurs. Typical values of the time needed to reach the equilibrium position lie in the order of 10^{-7} s to 10^{-6} s, and typical waiting times between

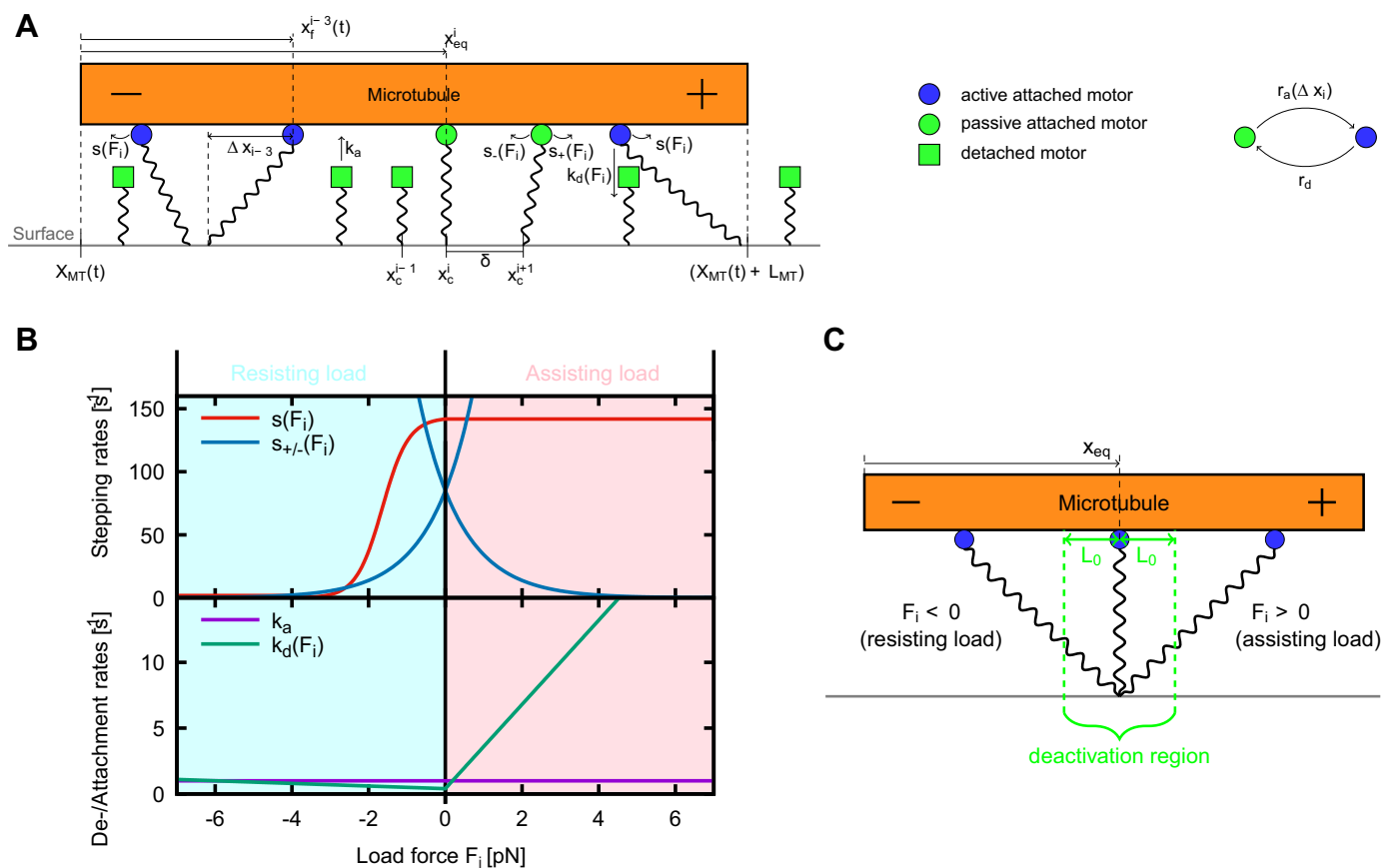


Fig. 2. Mathematical model. (A) The MT is represented as a rigid rod with minus and plus end. Motors are visualized as springs with squares (detached) or circles (attached) and are randomly distributed on the surface with mean distance δ . Passive attached motors are drawn in green, active attached motors in blue. Detached motors can bind with rate k_a to the MTs. Passive attached motors activate with rate $r_a(\Delta x_i)$ and become active attached motors, whereas active attached motors deactivate with rate r_d to become passive attached motors. Both active and passive attached motors detach with the force dependent rate $k_d(F_i)$. Passive attached motors step in both directions with rate $s_{\pm}(F_i)$ ('+' for stepping towards the MT plus end, '-' for stepping towards the MT minus end). Active attached motors walk with $s(F_i)$ toward the MT minus end until stall (see example of the leftmost active motor) and above stall towards the MT plus end (see example of the rightmost active motor). (B) Upper panel: dependence of the stepping rates on the load force for active attached motors $s(F_i)$ and passive attached motors $s_{\pm}(F_i)$. Passive attached motors have an enhanced/reduced stepping rate $s_{\pm}(F_i)$ for stepping towards/away from their equilibrium position x_{eq} , taking into account the harmonic potential of the motor spring. The stepping rate of active attached motors $s(F_i)$ has three different force regimes: for resisting forces above stall (strong negative force), the stepping rate is constant and low; for resisting forces below stall (smaller negative force), the stepping rate is monotonically increasing; and for assisting forces, the stepping rate is constant and high (see Materials and Methods for more details). Lower panel: dependence of the detachment rates for attached motors (active and passive) and the attachment rates for detached motors on the load force. The detachment rate $k_d(F_i)$ grows linearly with the load force in both directions, where the growth is faster for assisting forces than for resisting forces (Cleary et al., 2014). The attachment rate k_a of detached motors is independent of the load force. The load force is calculated from the motors' stretching (see Eqns 3, 4 and 5). (C) Scheme of the direction of the load force on the dynein motors, the corresponding sign of the load force and the deactivation region. Passive attached motors can be activated when the motors are stretched further than L_0 (i.e. outside the deactivation region).

two motor events are in the order of 10^{-4} s to 10^{-2} s. The system is updated by means of Gillespie's algorithm for time-independent rates (Gillespie, 1977). Possible update events are as follows:

Attachment

A detached motor attaches to the MT with rate k_a at its equilibrium position x_{eq}^i (MT system) if the corresponding site on the MT is not occupied. In our one-dimensional model, the motor's equilibrium position x_{eq}^i (in the MT system) corresponds to the position where $\Delta x_i = 0$.

Detachment

An attached motor detaches from the MT with the force-dependent detachment rate $k_d(F_i)$ given in Cleary et al. (2014). The detachment rate grows linearly with the absolute value of the motor's load force, where the detachment rate grows faster for assisting loads compared with resisting loads (Fig. 2B).

(De)activation

In our model, we assume that a detached dynein motor attaches to the MT in a passive, diffusive state. A passive attached motor, which

stretches outside the deactivation region ($|\Delta x_i| > L_0$, see Fig. 2C, the length of the deactivation region L_0 is the unstretched motor length given by the experimental working distance of the MT gliding assay) around the motor's equilibrium position x_{eq}^i will be activated with rate

$$r_a(\Delta x_i) = r_a^0 \left[1 - \exp\left(-\frac{k_1 L_0^2 + k_2 (|\Delta x_i| - L_0)^2}{2k_B T}\right) \right], \quad (1)$$

following the Arrhenius law, and where k_1 is the dynein stiffness inside the deactivation region and k_2 is the dynein stiffness outside the deactivation region. The stiffness inside the deactivation region k_1 and the activation rate constant r_a^0 are *a priori* unknown parameters, which were tuned to obtain the number dependence of the diffusion constant (Fig. S3) and the number dependence of the MT velocity (Fig. 3), respectively. Because attached motors are mechanically coupled via the rigid MT, passive attached motors typically get stretched by the activity of the active attached motors that transport the MT. We note that if all motors attached to the MT are passive, individual ones can also be activated by the diffusive stepping of the other attached passive motors. An active attached motor, the stretching of which returns into the deactivation region, deactivates with rate r_d (also an *a*

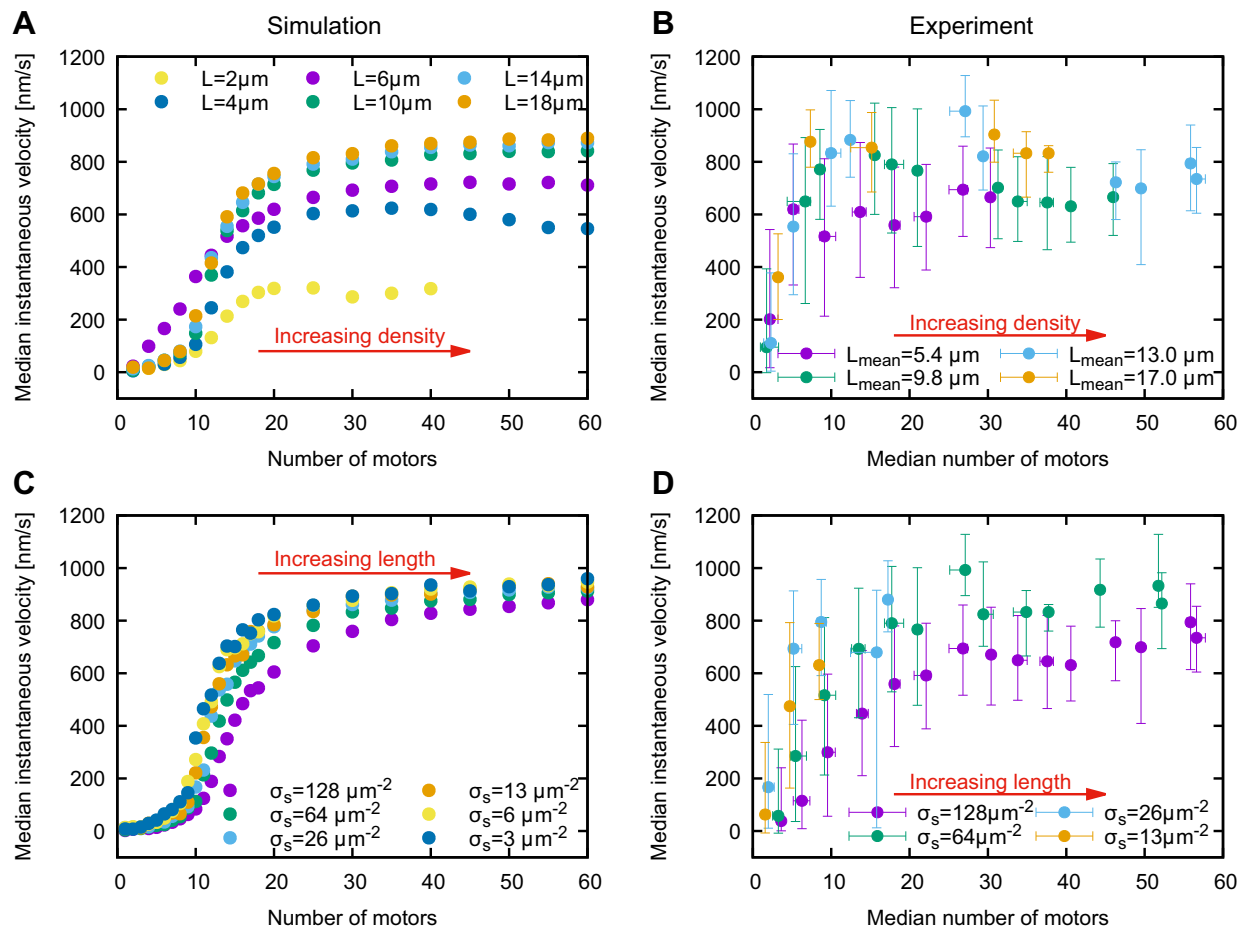


Fig. 3. Median instantaneous velocities with interquartile range as a function of motor number in simulation and experiment. (A–D) An increase in motor number was obtained by increasing the dynein surface density (A,B) or MT length (C,D). When increasing the motor number via the dynein surface density (A,B), the median velocity increased and saturated for all MT lengths. At higher motor numbers (above 20) a slight decrease of the median velocity became apparent especially in the experiment (B). For the same number of motors, a higher median velocity was observed for longer MTs. When increasing the motor number via the MT length, the median velocity increased and saturated for all dynein surface densities (C,D). The motor number in the experiment was estimated from the dynein surface density and the MT length and width (see Materials and Methods). Median and interquartile range of the experimental velocity distribution were chosen, as the velocity distribution was not Gaussian distributed (tested by Kolmogorov–Smirnov test). Each point of the simulation data is the median of $N=20,000$ data points.

priori unknown parameter, which is tuned to obtain the number dependence of the MT velocity).

Stepping

Any attached motor can perform steps of size d to neighboring, unoccupied sites on the MT. The stepping rate and direction depends on its load force and differs for active attached and passive attached motors (Fig. 2B). For an active attached motor, there are three different force regimes of the stepping rate $s(F_i)$: in the first case, the motor is attached at its equilibrium position x_{eq}^i or at a position towards the plus end. Hence, the motor is relaxed or pulled towards the MT minus end (assisting load) and the stepping rate is force independent. In accordance with the measured variance of the load-free dynein velocity, we have chosen Gaussian distributed forward velocities v_f assigned individually to each motor (see Materials and Methods). In the second case, the motor is attached at a position towards the minus end. Hence, the motor is pulled towards the MT plus end (resisting load) and the stepping rate decreases with increasing load until the motor stalls. In the third case, the resisting load is higher than the stall force and the motor steps toward the MT plus end with constant rate (backward stepping). Because there is no detailed description of the force dependency of active mammalian dynein, the Michaelis–Menten equation reported in Schnitzer et al. (2000) for kinesin is used. However, comparing the used stepping rates (Fig. 2B) with the force-velocity curve of Gennerich et al. (2007) for yeast dynein at 1 mM ATP (here, mammalian cytoplasmic dynein at 2 mM ATP), we see that the overall behavior is the same. A passive attached motor steps diffusively along the MT in both directions with rate $s_{\pm}(F_i)$ ('+' and '-' denoting movement towards the MT plus and minus end, respectively) taking into account the harmonic potential of the motor spring. The harmonic potential causes the rate for stepping away from the motor's equilibrium position to be reduced and the rate for stepping towards the equilibrium position to be enhanced. For the stepping rates in the harmonic potential, the Arrhenius law is used.

More details regarding the model and its computational implementation can be found in the Materials and Methods and the Supplementary Information.

Applying the described mathematical model and comparing the results to our experimental data, we first investigated the

dependence of the median instantaneous velocities as a function of the motor number (Fig. 3). Both in theory and experiment, we calculated the motor number (all motors that can potentially access the MT, i.e. the sum of active attached, passive attached and detached motors) from the estimated dynein surface density and the MT length (see Materials and Methods). When increasing the motor number via the dynein surface density (Fig. 3A,B), we observe a strong increase in the MT velocity for motor numbers up to 20. Upon further increase of the motor number, the MT velocity levels off and slows down. Interestingly, for a fixed number of motors we observe higher velocities for longer MTs. This finding is likely due to the fact that attached motors, once activated, can perform longer runs on longer MTs. The ratio of active attached to passive attached motors is thus expected to be higher on longer MTs (Fig. 4A). Moreover, for large numbers of motors on short filaments, i.e. high densities, the simulations and the experiments show a slight decrease in the median velocity. This effect indicates that at high motor densities, dynein motors mutually inhibit each other to step freely, e.g. due to steric repulsion. In the simulation, this phenomenon is modeled as an exclusion effect (i.e. at high motor densities an active attached motor might not freely step forward because the next binding site is blocked by another motor). Similar results are obtained when increasing the motor number via the MT length (Fig. 3C,D); the MT velocity increases as a function of the number of available motors, leveling off for more than 20 motors. From this representation, we can rule out a direct coupling of the dynein motors, because we observe high velocities even for small densities, i.e. at large distances between the dynein motors. This means that the MT velocity strongly depends on the number of attached motors indirectly, mechanically coupled via the rigid MT. This strengthens the assumption of a mechanical activation process via motor stretching. Furthermore, we do not see a significant slowing down for high motor numbers in this representation, which underscores that the slowing down at high motor densities is caused by a mutual inhibition of the motors, e.g. by steric repulsion.

We then applied our model to investigate the ratio of active attached to passive attached motors (further on denoted as motor activation ratio) as a function of motor number (Fig. 4 and Fig. S2 for the number dependence of the active attached and passive attached motors, respectively). When increasing the motor number via the

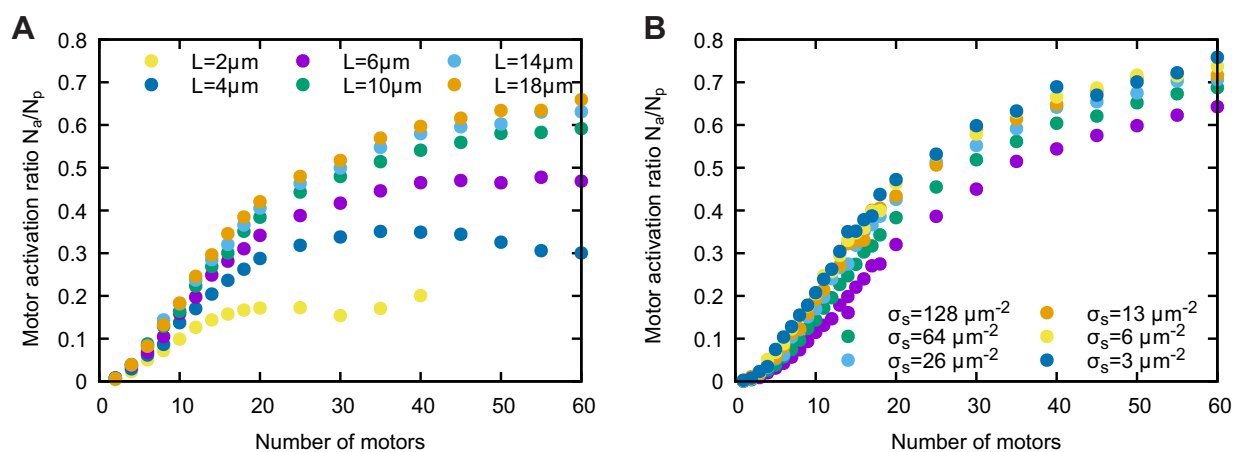


Fig. 4. Motor activation ratio as function of motor number. The motor number was increased via a change in motor density (A) or via a change in MT length (B). (A) The motor activation ratio first increases with motor number and then levels off or decreases. At a fixed motor number, the motor activation ratio is higher for longer MTs corresponding to higher velocities for longer MTs (Fig. 3A,B). (B) The motor activation ratio increases continuously with the motor number. At a fixed motor number, the motor activation ratio is lower for higher surface densities corresponding to lower velocities for higher surface densities (Fig. 3C,D). For each motor number and MT length/motor density, the number of data points is $N=20,000$.

dynein surface density (Fig. 4A), first an increase of the motor activation ratio with a subsequent leveling off or even a decrease (where exclusion effects become relevant) is observed. This result suggests that the dependence of the instantaneous velocity as a function of motor number (Fig. 3A,B) is directly influenced by the motor activation ratio. For a fixed number of motors, we observe a higher motor activation ratio for longer MTs corresponding to the observed higher velocities for longer MTs (Fig. 3A,B). When increasing the motor number via the MT length (Fig. 4B), a continuous increase and no leveling off of the motor activation ratio is observed. For a fixed number of motors, we observe a lower motor activation ratio for higher surface densities correlating to the observed lower velocities for higher surface densities (Fig. 3C,D). For a comparison of the instantaneous velocity histograms of the simulation and the experiment, see Fig. S1.

In order to emphasize the necessity of the activation process, we show median velocities in dependence of the motor number (Fig. 5), which were produced with an implementation of our model without the activation term. In this modified implementation, all motors (attached and detached) are always active. We see that the implementation without the activation term almost exclusively produces high MT velocities (Fig. 5). Only for very small MT lengths (high densities and low motor numbers in Fig. 5B), the MT velocity is not maximal owing to frequent de- and reattachment events.

Experiments and simulation were performed similarly for kinesin-1. There, gliding velocities were neither dependent on MT length nor kinesin-1 surface density. We therefore do not have an activation term in the mathematical model of kinesin-1. See Klein et al. (2014a) and the Materials and Methods for the kinesin-1 model, and Figs S4 and S5 for the experimental and simulation results of the kinesin-1 gliding assay.

DISCUSSION

Our results show that the number of available dynein motors influences the gliding motility of MTs. Experimentally, we demonstrated this number dependence by independently varying the MT length and the dynein surface density (Fig. 1). This behavior is in contrast to kinesin-1 gliding assays in which the MT length and the dynein surface density have no influence on the MT gliding velocity (Figs S4 and S5).

Previous experiments on single dynein motors have shown that, without adaptor proteins, single dynein is in an auto-inhibited state (McKenney et al., 2014; Schlager et al., 2014; Torisawa et al., 2014; Toropova et al., 2017; Zhang et al., 2017). The method of activation of single dynein by dynactin and adaptor proteins was recently revealed by cryo-electron microscopy (cryo-EM) (Toropova et al., 2017; Zhang et al., 2017). Dynactin binds to dynein and parallelly aligns its motor regions and therefore activates processive movement of single dynein motors (Zhang et al., 2017). It has been reported that applied force can also enable the processive stepping of individual cytoplasmic yeast dynein motors even in the absence of ATP (Gennerich et al., 2007). In addition, Torisawa et al. (2014) showed that physically separating the motor heads with a rigid rod leads to increased processivity. Therefore, we assume that motor stretching can bring the dynein out of the auto-inhibited (ϕ -stacked) state, in which the motor heads are closely stacked together. Here, we wondered whether such a mechanical activation alone could explain our results.

In our mathematical model, we therefore assumed a mechanical activation of dynein once it is sufficiently stretched (Fig. 2). This assumption, together with known results for the force-dependent stepping and detachment rates, allowed us to theoretically describe and reproduce the experimentally observed number dependence of dynein-driven motility (Fig. 3). We note that without the usage of motor activation, i.e. when dynein motors are permanently in an

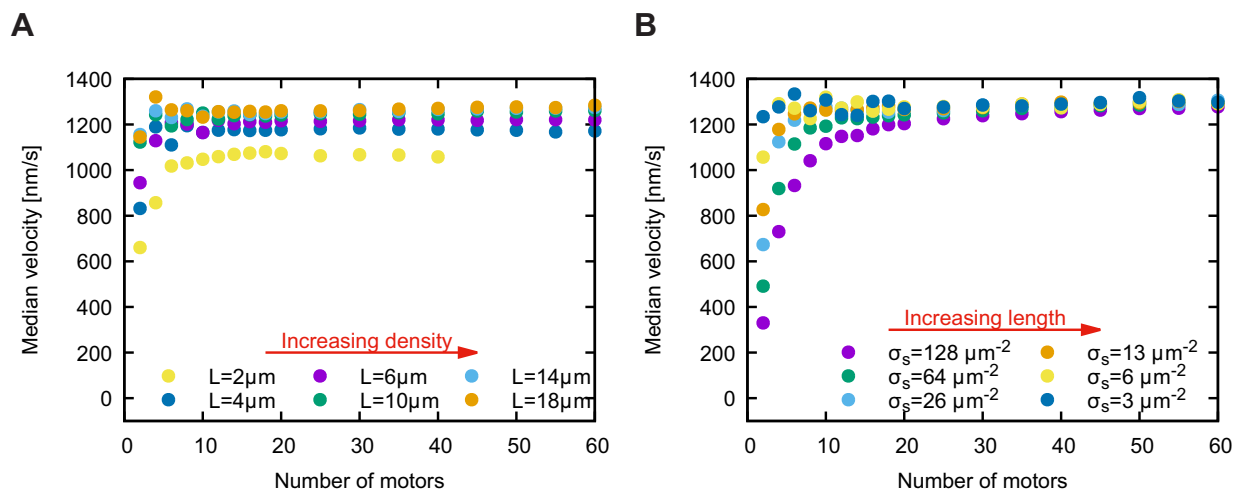


Fig. 5. Median velocities as a function of the motor number for a simulation without the mechanical activation term of the attached dynein motors. In this implementation of the mathematical model, all attached motors are in the active state. The active attached motors still step with the force-dependent stepping rate $s(F_i)$ and detach with the force-dependent detachment rate $k_d(F_i)$ and the detached motors attach the MT with the constant attachment rate k_a (same rate used for the detached motors in the unmodified simulation). (A) Median velocity as a function of the motor number for different MT lengths. The motor number was varied via the dynein surface density. High median velocities are observed for all motor numbers except for motor numbers of two. The reason for the high median velocities is the missing resistance of the passive attached motors. However, the median velocity for the shortest MTs ($L_{MT}=2 \mu\text{m}$) is reduced owing to a length effect. Although there is no activation process, the motors still detach at the end of the MT and new ones need to attach. Frequent detachment and attachment events slow down the MT. (B) Median velocity as a function of the motor number for different dynein surface densities. The motor number was varied via the MT length. For high dynein surface densities ($\sigma_s=128 \mu\text{m}^{-2}$ and $\sigma_s=64 \mu\text{m}^{-2}$), high median velocities are observed for motor numbers larger than six. The median velocities for motor numbers lower than six is reduced owing to the length effect (limited run length on short MTs for high densities and small motor numbers). For smaller dynein surface densities, high median velocities are observed for the whole range of motor numbers. High median velocities are due to the missing resistance of the passive attached motors. Each point is the median of $N=10,000$ data points.

active state (but still having all other dynein properties), we observe a kinesin-1-like behavior, which is characterized by high gliding velocities even for small motor numbers (Fig. 5).

The result that both gliding velocity and motor activation ratio increase with motor number (Figs 3 and 4), suggests that efficient transport of MTs depends on a high motor activation ratio. However, our simulation results show that this is only partly true: if the number of motors exceeds 20, the MT velocities saturate while the motor activation ratio further increases (as long as exclusion does not play a role). This result indicates that the impact of the resistance induced by the passive attached motors, which slows down the MT, becomes negligible at high motor numbers (above 20) and motor activation ratios. Furthermore, our theory predicts an influence of exclusion effects and the MT length on the MT velocity. We found that for a given number of motors in the MTs binding area, long MTs (experiencing a lower motor density than short MTs) glide faster than short MTs (Fig. 3A,C). One reason for this observation is that at lower motor densities, exclusion effects for the active motors are reduced. A similar slowdown of the gliding velocity at high motor densities has previously been observed for kinesin-14 (Hentrich and Surrey, 2018) and kinesin-1 (Bieling et al., 2008) motors. In addition to this, motors deactivate if they reach the end of the MT, where they detach. This effect limits the run lengths of active motors and lowers the motor activation ratio for short MTs, which then glide more slowly than long MTs. These predictions are confirmed by our experiments (Fig. 3B,D).

Besides activation, we found that in order to reproduce the experimentally observed velocity histograms with our mathematical model, it is necessary to consider a wide distribution of forward velocities for individual motors (Fig. S1). Assigning the same maximal velocity to all motors, we still can observe the dynein surface density and MT length dependence of the median MT velocity. However, the velocity histograms are then peaked around the mean value, whereas the experimentally found velocities are widely spread. The broad maximal velocity distribution is consistent with the velocity distributions of former single-molecule experiments (McKenney et al., 2014; Schlager et al., 2014), hinting to the fact that individual motors are not fully identical. This will be more the case in gliding motility assays, in which the actual attachment of each motor (e.g. its orientation with regard to the surface) might influence its stepping rate to a certain extent. Moreover, we see that the mean velocity of individual motors is higher than the highest observed median velocity of the gliding assay. The reason for this is presumably that the resistance of the passive attached motors slows down the motility of the active attached motors. The same effect can be seen in the experimental data of McKenney et al. (2014), in which both single-molecule stepping assay and gliding motility assay velocities of mammalian dynein motors are shown.

In earlier experimental studies, it has been suggested that motility powered by dynein is dependent on motor number and/or density. In experiments with bovine brain dynein bound to polystyrene beads, an improvement in motility was observed for cargo transport with higher motor numbers, which was explained by the suppression of an unproductive state (Mallik et al., 2005). It has also been shown that multiple mammalian cytoplasmic dynein coupled to DNA origami walked continuously, in contrast to single dynein motors (Torisawa et al., 2014). The authors of the latter study argued that single dynein molecules are in an auto-inhibited state and become active when assembled in a team. Lately, a dependence of the MT gliding velocity on the dynein surface density has been reported for monomeric as well as dimeric cytoplasmic dynein type 2, which is

intrinsically auto-inhibited similarly to dynein type 1 (Toropova et al., 2017). Also for axonemal inner arm dynein, an increase in velocity with motor number was observed (Sakakibara et al., 1999; Shimizu et al., 2014). However, the reasons for these behaviors have only been speculated about, and include cooperative activation (Torisawa et al., 2014) and an influence of the equilibrium between active and inactive forms of dynein (Torisawa et al., 2014; Toropova et al., 2017). It will be intriguing to test, by cryo-EM of motility assays with different motor activation ratios, whether our described activation of dynein by mechanical stretching leads to similar structural effects as adaptor activation and whether the presence of adaptor proteins further enhances the motility arising from multiple dynein motors.

Taken together, our results suggest that the gliding motility of dynein-driven MTs depends on the number of active motors attached to the filament. This number is determined by the total number of available motors as well as by their run length. Mechanical activation of individual dynein motors is key to our model, necessary to reproduce the experimental MT velocities as a function of motor number. In the future, it will be interesting to test the mathematical model for different experimental setups, including bidirectional cargo transport and transport in crowded environments.

MATERIALS AND METHODS

Flow channels

Experiments were performed in 1.5–3 mm-wide flow channels made from glass coverslips, which were held together by stripes of Parafilm. The coverslips were cleaned by the following procedure: (1) 15 min of sonication in 1:20 diluted detergent (Mucosal), (2) rinsing for 2 min with distilled water, (3) sonication in pure ethanol for 10 min, (4) rinsing for 2 min with distilled water, (5) rinsing for 2 min with double-distilled water and (6) blow drying with nitrogen.

Preparation of motor proteins and MTs

Cytoplasmic dynein expression and purification was performed as described previously (Schlager et al., 2014). Double-stabilized MTs were prepared by polymerization of partially rhodamine-labeled tubulin (in-house-prepared porcine brain tubulin, 4.6 mg/ml final concentration, labeling ratio 0.67) in BRB80 buffer with 1 mM MgCl₂, 1 mM guanylyl 50- α , β -methylene diphosphonate (GMPCPP) at 37°C overnight. The MTs were spun down in an ultracentrifuge for 10 min at 120,000 g (room temperature) to remove free tubulin. The MTs were re-suspended and stabilized in BRB80 containing 10 μ M Taxol.

Gliding motility assay

In all gliding assays, a dilution buffer (10 mM Pipes, 50 mM K-acetate, 4 mM MgSO₄, 1 mM EGTA, pH 7.0) with 0.1% Tween 20, 10 μ M Taxol, 2 mM MgATP and 10 mM dithiothreitol was used. Before every experimental day a one-step affinity pull-down of dynein was performed, incubating dynein with unlabeled MTs in dilution buffer supplemented by 2 mM ATP. Spinning down the solution in an ultracentrifuge for 10 min at 120,000 g (room temperature) reduced the amount of dysfunctional rigor-binding motors, and the supernatant was used for the experiment. For preparation of the channels, the following protocol was utilized: a solution containing 2.5 mg/ml protein A in ddH₂O was perfused into the channel and incubated for 5 min. The channels were then washed with dilution buffer. Solutions containing different concentration of dynein were perfused into the channel and incubated for 5 min. In the next step, a solution containing 500 μ g/ml casein was flushed into the channels and incubated for 5 min. The channels were then washed with dilution buffer. A motility solution (40 mM glucose, 110 μ g/ml glucose-oxidase, 10 μ g/ml catalase in dilution buffer) containing double-stabilized MTs was perfused into the channel and incubated for 1 min. Finally, a motility solution without MTs was applied.

The surface density of dynein motors was estimated based on the assumption that 10% of the motor proteins perfused into the flow cell (7 μl) did bind to the surfaces of the flow cell ($2 \times 18 \times 3 \text{ mm}^2$) in such a manner that they were capable of constructively contributing to MT transport. The other motors might not have bound to the surfaces, or might have bound in a configuration in which they neither contributed to nor hindered MT transport [see also Kotani et al. (2007) for similar arguments with regard to MT motility on surfaces coated by axonemal dynein-f and dynein-c]. Applying dynein concentrations of 55, 28, 11, 6, 3 and 1.5 $\mu\text{g/ml}$ thus yielded estimated surface densities of 128, 64, 26, 13, 6 and 3 μm^{-2} , respectively. We are aware that these surface densities are rough estimates only. However, we confirmed the linear relationship between applied motor concentration and surface density by landing rate measurements (according to Agarwal et al., 2012; Katira et al., 2007). Specifically, for the motor concentrations of 55, 28, 11 and 6 $\mu\text{g/ml}$ applied in the quantitative comparisons of Fig. 3, we obtained surface densities of 39, 20, 8, and 4 μm^{-2} .

Imaging

Gliding MTs were imaged using an inverted fluorescence microscope (Axiovert 200M; Zeiss) with a $40 \times$ oil immersion objective (NA 1.3) and an objective heater set to 27°C . For illumination, a metal arc lamp (Lumen 200; Prior Scientific) and filter sets for rhodamine were utilized (excitation, 535/50; dichroic, LP 565; emission, 610/75). An iXon Ultra EMCCD (Andor) was used for image acquisition, and timelapse movies of 200 frames with 100 ms exposure time at a frame rate of 1 Hz were acquired using MetaMorph software (Universal Imaging). Experiments were repeated in several independent sets of gliding assays (more than three) and similar results were obtained.

Data analysis

For filament tracking and path statistics, Fluorescence Image Evaluation Software for Tracking and Analysis (FIESTA) (Ruhnow et al., 2011) was used. FIESTA uses Gaussian models to find and track the filaments. All MT tracks were visually inspected and data points for which the MT length significantly varied between consecutive frames (e.g. owing to MTs crossing each other) were discarded. Instantaneous velocities were determined by calculating one-dimensional velocities v_i using the difference quotient of the distance along the path and the time between consecutive frames for each MT in the field of view at each point of time and adding a gliding average of three consecutive velocities $v_i^g = (v_{i-1} + v_i + v_{i+1})/3$. For the histograms of instantaneous velocities of Fig. 1 MATLAB (MathWorks) was used. One-dimensional velocities v_i with a time difference greater than 1.5 s were discarded owing to an assumed tracking error. Median velocities and quartiles of the velocity distributions were calculated (with a self-written C++ program) using the following calculation rules: the median for an even number of data points N is calculated by $\tilde{v} = (v_m + v_{m-1})/2$, where the middle is $m = N/2$, and for an odd number of data points by $\tilde{v} = v_m$, where the middle is $m = \lfloor N/2 \rfloor$. The interquartile ranges for $N/4$ being an integer value are calculated by $v_{0.25} = (v_{N/4-1} + v_{N/4})/2$ and $v_{0.75} = (v_{3N/4-1} + v_{3N/4})/2$, and those for a noninteger value are calculated by $v_{0.25} = v_{\lfloor N/4 \rfloor}$ and $v_{0.75} = v_{\lfloor 3N/4 \rfloor}$. The number of data points N is defined as the product of the number of MTs in the considered range times the number of frames of that corresponding MT.

Details of the dynein gliding assay simulation

Theoretical set-up: the motors are uniformly distributed on the surface with distances between $2R$ and $\delta - 2R$, where R denotes the radius of the dynein motor and δ the mean distance between two motors (everything in the surface system). The mean distance is calculated as follows:

$$\delta = \frac{L_{MT}}{N} = \frac{L_{MT}}{L_{MT} \cdot L_0 \cdot \sigma_s} = \frac{1}{L_0 \cdot \sigma_s}, \quad (2)$$

where N is the average number of motors that can bind to a MT of length L_{MT} . Here, it is assumed that all the motors within the area $L_{MT} \cdot L_0$ can attach to the MT. For the dynein surface density σ_s , the experimentally estimated values are applied. The position of the i^{th} motor's tail on the surface is

denoted by x_c^i (surface system) and the position of the i^{th} motor's head on the MT by $x_f^i(t)$ (MT system). $x_f^i(t)$ ranges from 0 (MT minus end) to L_{MT} (MT plus end). The position of the MT minus end in the surface system is denoted by $X_{MT}(t)$ (Fig. 2A).

Force calculation: for dynein, we assume two force regimes. If dynein's stretching is inside the deactivation area, the force is calculated by:

$$F_i = k_1(\Delta x_i), \quad (3)$$

where k_1 is the stiffness of the motor inside the deactivation region. If dynein's stretching is outside the deactivation area, the force is calculated by:

$$F_i = -k_1 L_0 + k_2(\Delta x_i + L_0) \quad (4)$$

for the case $\Delta x_i < 0$ and by

$$F_i = k_1 L_0 + k_2(\Delta x_i - L_0) \quad (5)$$

for the case $\Delta x_i > 0$. k_2 is the stiffness of the motor outside the deactivation region.

Attachment: see Results.

Detachment: the detachment rates of the dynein motors are based on Cleary et al. (2014). They are calculated as:

$$k_d(F_i) = \begin{cases} -0.1F_i + 0.4 & \text{for } F_i \leq 0 \\ 3.2F_i + 0.4 & \text{for } F_i > 0 \end{cases} \quad (6)$$

(De)activation: see Results.

Stepping: if the neighboring site is empty the dynein motor performs a step of size d . The stepping is different for active and passive motors.

Active motor: if the load force is greater than or equal zero (assisting load) the stepping rate is:

$$s(F_i) = \frac{[\text{ATP}] \cdot v_f/d}{[\text{ATP}] + v_f/(1.3d)}, \quad (7)$$

with the forward velocity v_f being Gaussian distributed around $v_{f,\text{mean}}$ and with standard deviation σ_v . We truncated the Gaussian distribution at $v_{f,\text{lowest}}$ and $v_{f,\text{highest}}$ to avoid unrealistic velocities. If the load force is less than zero (resisting load) but still greater than the negative of the stall force, the stepping rate decreases with load:

$$s(F_i) = \frac{k_{cat}(F_i) \cdot [\text{ATP}]}{[\text{ATP}] + (k_{cat}(F_i)/k_b(F_i))} \quad (8)$$

with

$$k_j(F_i) = \frac{k_j^0}{p + q \cdot \exp(F_i \delta_c / (k_B T))} \quad j \in \{b, cat\}. \quad (9)$$

Here, δ_c is the characteristic distance and k_j^0 the unloaded rate constant. In the last case, the load force is less than the stall force (high resisting load) and the motor steps backward (towards the plus end) with constant rate $s(F_i) = v_b/d$. The ATP and load force dependency for the active motor stepping are taken from Schnitzer et al. (2000).

Passive motor: passive motors diffuse in a harmonic potential, where the stepping towards the motor's equilibrium position is enhanced and the stepping away from the motor's equilibrium position is reduced. For the stepping in the harmonic potential $s_{\pm}(F_i)$ the Arrhenius law is used:

$$s_{\pm}(F_i) = s_0 \cdot \exp\left(\mp \frac{F_i \cdot d}{2 \cdot k_B T}\right), \quad (10)$$

where 's₊' denotes stepping towards the MT plus end and 's₋' stepping towards the MT minus end. The parameter s_0 resembles the force-free stepping rate and was estimated from the diffusion coefficient. See Fig. S3 for the dependence of the diffusion coefficient on the motor number for experiment as well as simulation.

Program run

Initialization: first, all the motors are distributed on the surface. At the beginning, the MT is at position $X_{MT}(t=0)=0$ and no motor is attached to the MT.

Update: Gillespie's algorithm with the first reaction method is used to choose the next event out of all possible events. Then the chosen event is performed and the MT is moved to the equilibrium position.

Measurement: after the relaxation time ($t > t_{relax}$), each second the MT position is measured and stored. For the MT position, a Gaussian distribution around the simulation MT position is applied to mimic the experimental measurement uncertainty. The standard deviation of the Gaussian is denoted by σ_{pos} . From the MT position, the instantaneous velocity is calculated by using the difference quotient of the moved distance and the corresponding time difference with respect to the previous measurement. All measured instantaneous velocities are stored and output.

Termination: one run is terminated if the time is bigger than t_{end} or if all motors are detached. If no motor is attached to the MT in the experiment, the MT will diffuse away and the measurement of the MT position will stop. The whole program is terminated when $N_{samples}$ runs were performed. At the end of the program, the mean velocity as well as the mean numbers of active and passive attached motors are output and stored.

Data processing: from the stored instantaneous velocities median velocities and quartiles as well as histograms of velocity gliding averages are calculated as described in the 'Data analysis' section.

Model parameters

In Table S1, all model parameters are listed and it is explained how the used values were obtained (unknown, estimated from, related to earlier studies, etc). References to earlier studies were made wherever possible.

The kinesin-1 model

The simulation of the kinesin-1 gliding assay setup is the same as previously described for the dynein assay. The used mathematical model for the molecular motor is the kinesin-1 model described in Klein et al. (2014a), with a modified force-dependent detachment behavior. Here, we used a purely exponentially growing detachment rate:

$$k_d(F_i) = k_d^0 \cdot \exp\left(\frac{|F_i|}{F_d}\right) \quad (11)$$

(slip bond behavior).

Furthermore, we adjusted the applied parameter values to the current state of art values (see Table S1 for the parameter values).

Acknowledgements

We thank Andrew Carter for kindly providing the plasmid of the recombinant mammalian cytoplasmic dynein; Wim Walter for performing initial dynein gliding assays; C. Bräuer for technical assistance; and Sarah Klein for initial support on the simulation of dynein gliding assays.

Competing interests

The authors declare no competing or financial interests.

Author contributions

Conceptualization: G.A.M., L. Scharrel, L. Santen, S.D.; Formal analysis: G.A.M., L. Scharrel, L. Santen, S.D.; Investigation: G.A.M., L. Scharrel, L. Santen, S.D.; Resources: L. Scharrel, S.D.; Data curation: G.A.M., S.D.; Writing - original draft: G.A.M., L. Scharrel, L. Santen, S.D.; Writing - review & editing: G.A.M., L. Scharrel, L. Santen, S.D.; Visualization: G.A.M., L. Scharrel; Supervision: L. Santen, S.D.; Project administration: L. Santen, S.D.; Funding acquisition: L. Santen, S.D.

Funding

This work was supported by Deutsche Forschungsgemeinschaft (SFB1027) and Technische Universität Dresden.

Supplementary information

Supplementary information available online at <http://jcs.biologists.org/lookup/doi/10.1242/jcs.220079.supplemental>

References

- Agarwal, A., Luria, E., Deng, X., Lahann, J. and Hess, H. (2012). Landing rate measurements to detect fibrinogen adsorption to non-fouling surfaces. *Cell. Mol. Bioeng.* **5**, 320-326.
- Belyy, V., Schlager, M. A., Foster, H., Reimer, A. E., Carter, A. P. and Yildiz, A. (2016). The mammalian dynein-dynactin complex is a strong opponent to kinesin in a tug-of-war competition. *Nat. Cell Biol.* **18**, 1018-1024.
- Bieling, P., Telley, I. A., Piehler, J. and Surrey, T. (2008). Processive kinesins require loose mechanical coupling for efficient collective motility. *Eur. Mol. Biol. Org. Rep.* **9**, 1121-1127.
- Bieling, P., Kronja, I. and Surrey, T. (2010). Microtubule motility on reconstituted meiotic chromatin. *Curr. Biol.* **20**, 763-769.
- Cleary, F. B., Dewitt, M. A., Bilyard, T., Min Htet, Z., Belyy, V., Chan, D. D., Chang, A. Y. and Yildiz, A. (2014). Tension on the linker gates the ATP-dependent release of dynein from microtubules. *Nat. Commun.* **5**, 4587.
- Derr, N. D., Goodman, B. S., Jungmann, R., Leschziner, A. E., Shih, W. M. and Reck-Peterson, S. L. (2012). Tug-of-war in motor protein ensembles revealed with a programmable DNA origami scaffold. *Science* **338**, 662-665.
- Gennerich, A., Carter, A. P., Reck-Peterson, S. L. and Vale, R. D. (2007). Force-induced bidirectional stepping of cytoplasmic dynein. *Cell* **131**, 952-965.
- Gillespie, D. T. (1977). Exact stochastic simulation of coupled chemical reactions. *J. Phys. Chem.* **81**, 2340-2361.
- Hentrich, C. and Surrey, T. (2018). Microtubule organization by the antagonistic mitotic motors kinesin-5 and kinesin-14. *J. Cell Biol.* **189**, 465-480.
- Katira, P., Agarwal, A., Fischer, T., Chen, H.-Y., Jiang, X., Lahann, J. and Hess, H. (2007). Quantifying the performance of protein-resisting surfaces at ultra-low protein coverages using kinesin motor proteins as probes. *Adv. Mater.* **19**, 3171-3176.
- Klein, S., Appert-Rolland, C. and Santen, L. (2014a). Environmental control of microtubule-based bidirectional cargo transport. *EPL* **107**, 18004.
- Klein, S., Appert-Rolland, C. and Santen, L. (2014b). Fluctuation effects in bidirectional cargo transport. *Eur. Phys. J. Spec. Top.* **223**, 3215-3225.
- Kotani, N., Sakakibara, H., Burgess, S. A., Kojima, H. and Oiwa, K. (2007). Mechanical properties of inner-arm dynein-f (dynein i1) studied with in vitro motility assays. *Biophys. J.* **93**, 886-894.
- Larson, A. G., Landahl, E. C. and Rice, S. E. (2009). Mechanism of cooperative behaviour in systems of slow and fast molecular motors. *Phys. Chem. Chem. Phys.* **11**, 4890-4898.
- Mallik, R., Petrov, D., Lex, S. A., King, S. J. and Gross, S. P. (2005). Building complexity: an in vitro study of cytoplasmic dynein with in vivo implications. *Curr. Biol.* **15**, 2075-2085.
- McKenney, R. J., Huynh, W., Tanenbaum, M. E., Bhabha, G. and Vale, R. D. (2014). Activation of cytoplasmic dynein motility by dynactin-cargo adapter complexes. *Science* **345**, 337-341.
- Nicholas, M. P., Höök, P., Brenner, S., Wynne, C. L., Vallee, R. B. and Gennerich, A. (2015). Control of cytoplasmic dynein force production and processivity by its c-terminal domain. *Nat. Commun.* **6**, 6206.
- Pan, X., Ou, G., Civelekoglu-Scholey, G., Blacque, O. E., Endres, N. F., Tao, L., Mogilner, A., Leroux, M. R., Vale, R. D. and Scholey, J. M. (2006). Mechanism of transport of IFT particles in *C. elegans* cilia by the concerted action of kinesin-II and OSM-3 motors. *J. Cell Biol.* **174**, 1035-1045.
- Ruhnow, F., Zwicker, D. and Diez, S. (2011). Tracking single particles and elongated filaments with nanometer precision. *Biophys. J.* **100**, 2820-2828.
- Sakakibara, H., Kojima, H., Sakai, Y., Katayama, E. and Oiwa, K. (1999). Inner-arm dynein c of *Chlamydomonas* flagella is a single-headed processive motor. *Nature* **400**, 586-590.
- Scharrel, L., Ma, R., Schneider, R., Jülicher, F. and Diez, S. (2014). Multimotor transport in a system of active and inactive kinesin-1 motors. *Biophys. J.* **107**, 365-372.
- Schlager, M. A., Hoang, H. T., Urnavicius, L., Bullock, S. L. and Carter, A. P. (2014). In vitro reconstitution of a highly processive recombinant human dynein complex. *EMBO J.* **33**, 1855-1868.
- Schnitzer, M. J., Visscher, K. and Block, S. M. (2000). Force production by single kinesin motors. *Nat. Cell Biol.* **2**, 718-723.
- Shimizu, Y., Sakakibara, H., Kojima, H. and Oiwa, K. (2014). Slow axonemal dynein e facilitates the motility of faster dynein c. *Biophys. J.* **106**, 2157-2165.
- Tanenbaum, M. E., Vale, R. D. and McKenney, R. J. (2013). Cytoplasmic dynein crosslinks and slides anti-parallel microtubules using its two motor domains. *eLife* **2**, e00943.
- Torisawa, T., Ichikawa, M., Furuta, A., Saito, K., Oiwa, K., Kojima, H., Toyoshima, Y. Y. and Furuta, K. (2014). Autoinhibition and cooperative activation mechanisms of cytoplasmic dynein. *Nat. Cell Biol.* **16**, 1118-1124.
- Toropova, K., Mladenov, M. and Roberts, A. J. (2017). Intraflagellar transport dynein is autoinhibited by trapping of its mechanical and track-binding elements. *Nat. Struct. Mol. Biol.* **24**, 461-468.
- Zhang, K., Foster, H. E., Rondelet, A., Lacey, S. E., Bahi-Buisson, N., Bird, A. W. and Carter, A. P. (2017). Cryo-EM reveals how human cytoplasmic dynein is auto-inhibited and activated. *Cell* **169**, 1303-1314.e18.

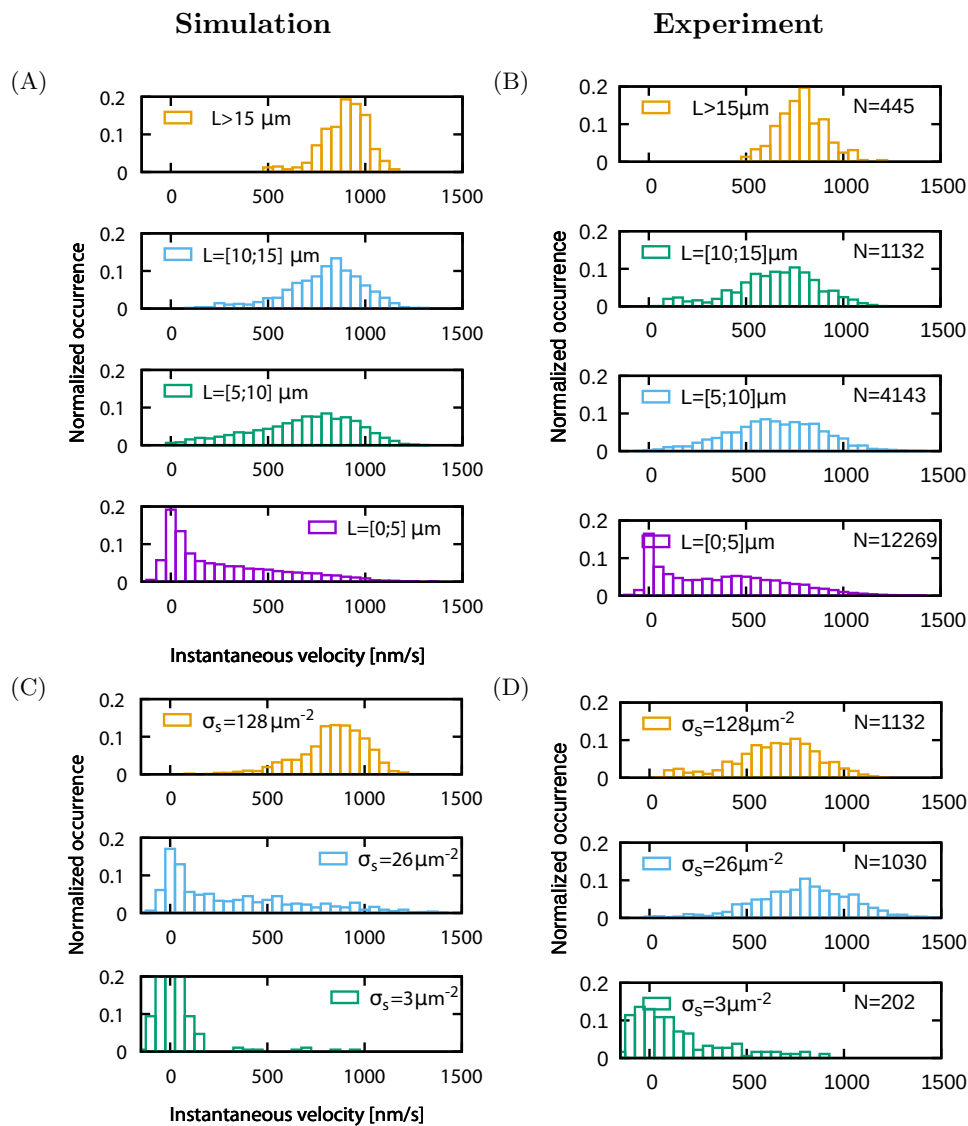


Figure S1: Normalized histograms of instantaneous MT velocities for different MT lengths (figure S1A and S1B) and dynein surface densities (figure S1C and S1D) from the simulation (left) and the experiment (right). For figure S1A and S1B the dynein surface density is constant ($\sigma_s = 128 \mu\text{m}^{-2}$) and for figure S1C and S1D the MT lengths are all between $10 \mu\text{m}$ and $15 \mu\text{m}$. The number of datapoints N is given in the upper right corner of the experimental histograms. In the simulation a similar number of datapoints is applied for each case, respectively.

The simulation (figure S1A) resembles the experimental length dependence (figure S1B) of the velocity histograms. Histograms of the dynein surface density dependence for the simulation (figure S1C) and for the experiment (figure S1D) are in agreement for low ($\sigma_s = 3 \mu\text{m}^{-2}$) and high ($\sigma_s = 128 \mu\text{m}^{-2}$) motor densities. (*Continuation on next page.*)

Figure S1 (*previous page*): However, at intermediate dynein surface density ($\sigma_s = 26 \mu\text{m}^{-2}$) the simulated distribution is peaked around zero with a tail towards high velocities while the experimental distribution is widely spread at high velocities. This discrepancy is likely due to the uncertainty in our experimental estimates with regard to the motor surface density, coupled with a high sensitivity of the behavior of our transport system to slight variations in surface density at $\sigma_s = 26 \mu\text{m}^{-2}$ (see Figure 3D of the main text). Note that in order to reproduce the velocity histograms the same number of trajectories as in the experiments are simulated with regards to the number of measurements and the mean MT lengths.

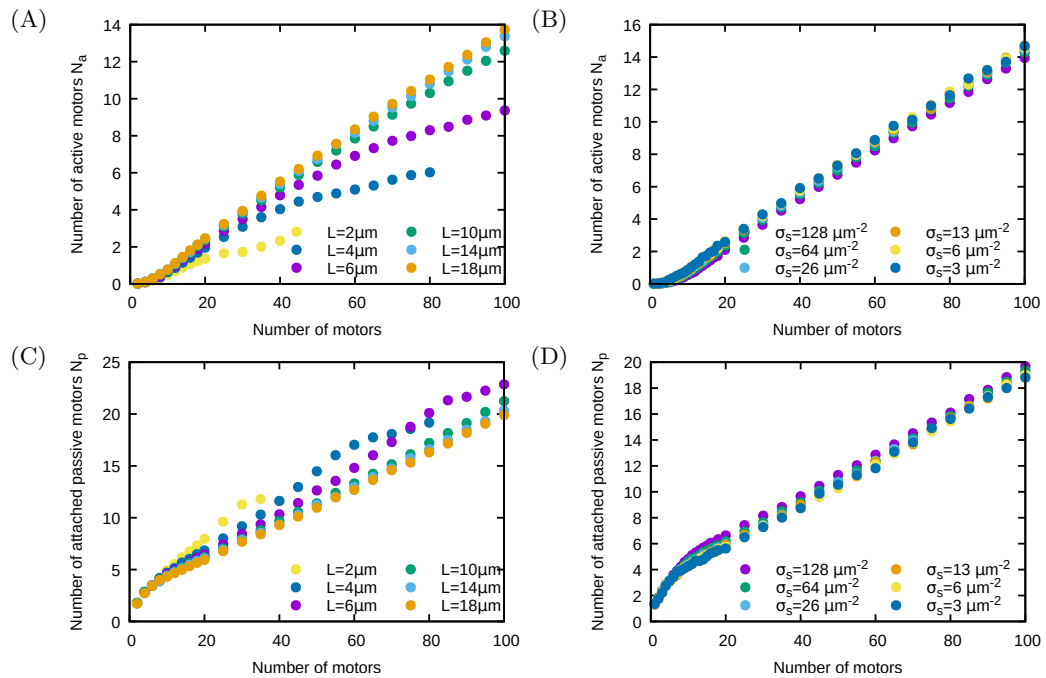


Figure S2: Figures S2A and S2B show the number of active attached motors and figures S2C and S2D the number of passive attached motors in dependence of the total number of motors for the simulation. In figure S2A and S2C the motor number is varied via the dynein surface density and in S2B and S2D via the MT length.

In figure S2A the number of active attached motors increases linearly with the motor number as long as exclusion effects are negligible (orange, light blue and green). At constant dynein surface density (figure S2B) the number of active attached motors increases linearly with the number of motors even for high number of motors.

In figure S2C the number of passive attached motors increases linearly with the motor number as well as long as exclusion effects are negligible (orange, light blue and green). At the point where exclusion effects become relevant the number of passive attached motors increases faster. At constant dynein surface density (figure S2D) the number of passive attached motors increases linearly with the number of motors as well. At very low number of motors, the majority of attached motors are in a passive state.

For each motor number and MT length/motor density the number of data-points is $N = 20.000$

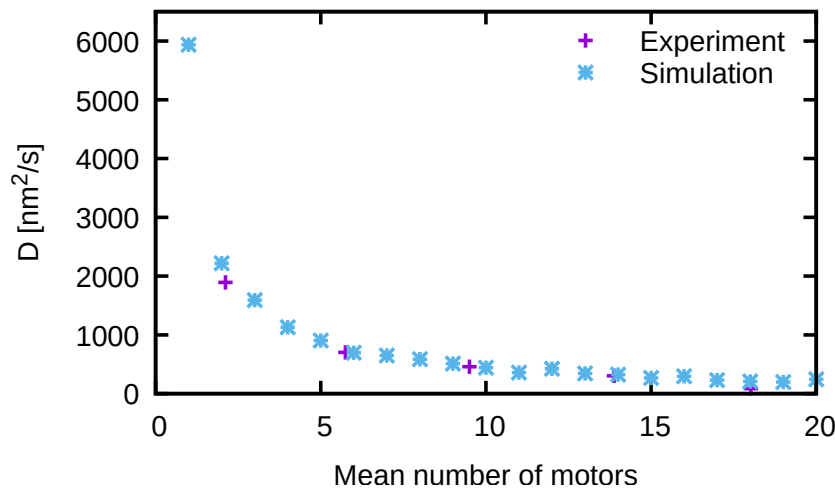


Figure S3: Diffusion coefficient of surface-bound MTs as function of the mean number of motor for experiment as well as simulation. In the experiment at low motor numbers the MT is not transported over longer distances but slightly moved back- and forward. We assume that in this case only passive motors are attached, which diffuse in the harmonic potential of the motor’s spring. We call this state ”bound MT diffusion”. The higher the number of attached motors, the higher is the chance for the motors to activate and the lower is the diffusion part of the MT motion. In [15] a similar behavior can be seen in dependence of the number of motors. However, the diffusion coefficients found in [15] are around 4 – 5 times higher than the ones of our experiment. Calculation of the diffusion coefficients were performed as follows.

Experiment: For the experimental data it is assumed that all measured negative velocities belong to the bound MT diffusion and are produced by the diffusive stepping of the passive attached motors. Mirroring the distribution of the negative velocities and applying a Gaussian fit, we calculated the variance of the velocities of the bound MT diffusion $\sigma_v^2 = \langle v^2 \rangle (\langle v \rangle = 0$ because of the mirroring). Due to a constant time difference ($\Delta t \approx 1$ s), which is used to calculate the instantaneous velocities, and a zero mean ($\langle x \rangle = 0$) we can express the mean square displacement in terms of the variance of the velocity. The expression is obtained as follows:

The instantaneous velocity is given by $v = (\Delta x) / (\Delta t)$. Since we consider an unbiased diffusion, we have $\langle x \rangle = \langle v \rangle = 0$. Therefore (and because of the constant time difference Δt), the variance of the velocity is given by $\langle v^2 \rangle = \langle (\Delta x)^2 \rangle / (\Delta t)^2$. For the same reason the mean square displacement can be expressed as $\langle x^2 \rangle = n \langle (\Delta x)^2 \rangle$, where n is the number of datapoints defined by the time difference Δt and the total time $t = n\Delta t$. Taking everything together we find $\langle x^2 \rangle = t (\Delta t) \langle v^2 \rangle$. Using the mean square displacement in standard one-dimensional diffusion $\langle x^2 \rangle = 2Dt$, (*Continuation on next page.*)

Figure S3 (*previous page*): we then find for the diffusion constant the expression: $D = \frac{\langle v^2 \rangle}{2} \Delta t$.

Simulation: We assume that the observed diffusive motion of the experiment has its origin in the diffusive stepping of the passive attached motors. In order to fit the diffusion constant of the experiment we implemented the diffusive stepping in the harmonic potential of the motor's springs in a small extra implementation. In this implementation periodic boundary conditions of the MT system were applied (meaning that the MT minus end and the MT plus end are the same points) and the motors are all passive and attached to the MT. (No active attached or passive detached motors exist.) In this set-up the MT diffuses in the harmonic potential of the motors springs, which is a stochastic process in thermal equilibrium. In order to take the energy landscape into account the Metropolis algorithm is applied [11]. We run the simulation for different motor numbers and calculate the diffusion constant for each of them by fitting the time-dependence of the mean square displacement ($N = 400$ samples for each measurement timepoint, 500 timepoints) of the MT trajectories ($t_{\text{start}} = 50$ s and $t_{\text{end}} = 550$ s). In order to adjust the curve of the experimental data we optimized the force-free stepping rate of the passive attached motors (denoted by s_0) and the stiffness of the dynein motor k_1 (stiffness for motor's stretchings inside the deactivation region).

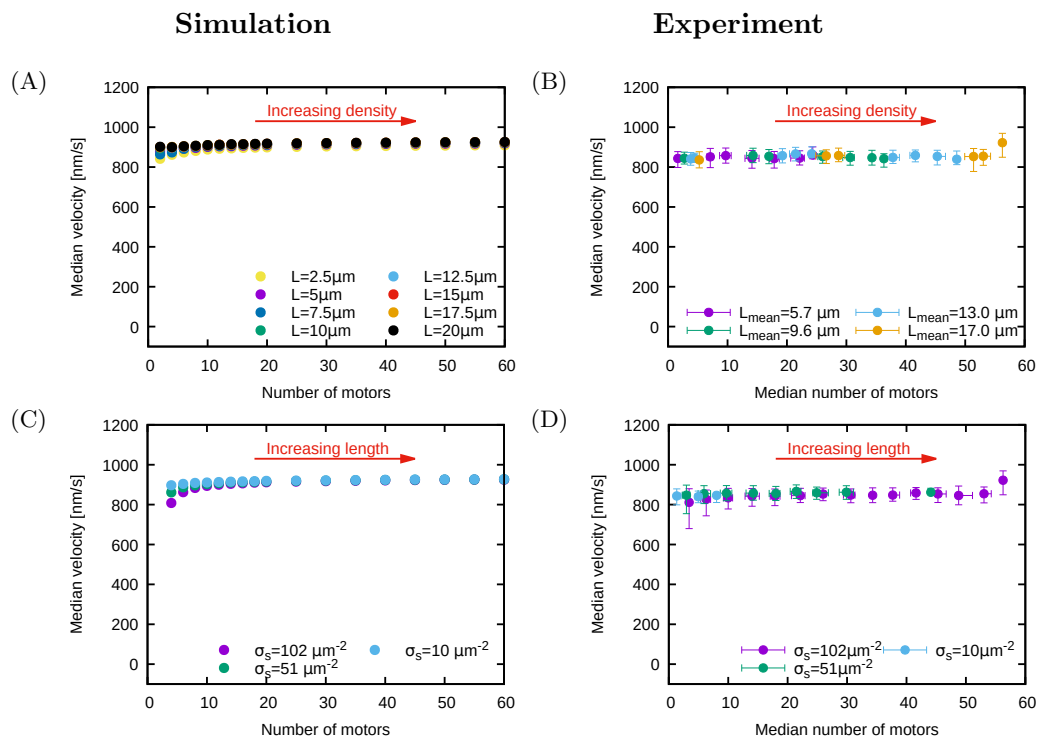


Figure S4: Median velocity (plus interquartile range for the experiment) of the kinesin-1 gliding assay of the simulation (left) and the experiment (right). In figure S4A and S4B the median velocity for different lengths is shown while the number of motors is varied via the kinesin-1 surface density. In figure S4C and S4D the median velocity is shown for different kinesin-1 surface densities while the number of motors is varied via the MT length. For the MT length dependence (figure S4C and S4D) as well as for the kinesin-1 surface density dependence (figure S4A and S4B) constant high median MT gliding velocities were observed for the simulation as well as for the experiment.

Each point of the simulation data is the median of $N = 10.000$ datapoints.

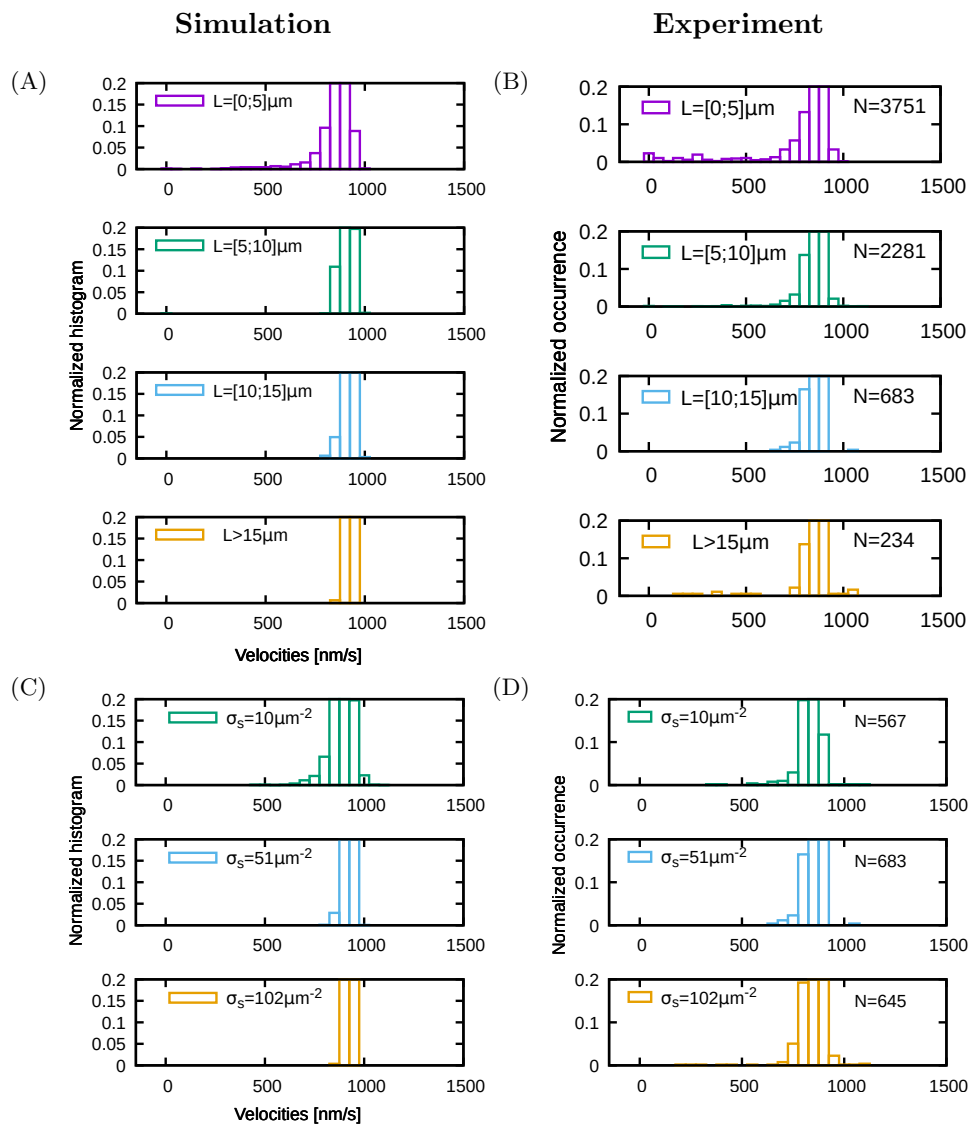


Figure S5: Normalized histograms of instantaneous MT velocities for different MT lengths (figure S5A and S5B) and kinesin-1 surface densities (figure S5C and S5D) from the simulation (left) and the experiment (right). For figure S5A and S5B the kinesin-1 surface density is constant ($\sigma_s = 51 \mu\text{m}^{-2}$) and for figure S5C and S5D the MT lengths are all between 10 μm and 15 μm . The number of datapoints N is given in the upper right corner of the experimental histograms. In the simulation a similar number of datapoints is applied for each case, respectively.

For simulation and experiment and at all MT lengths and kinesin-1 surface densities velocity distributions with a sharp peak at high velocities are observed.

Description	Value	Reference and further Explanation
Common parameters:		
Length of the deactivation region	$L_0 = 30 \text{ nm}$	Is equal the unstretched motor length given by the experimental working distance of the MT gliding assay
Stepsize	$d = 8 \text{ nm}$	[3, 16, 8]
ATP concentration	$[\text{ATP}] = 2000 \mu\text{M}$	Given by the experiment
Relaxation time	$t_{\text{relax}} = 20 \text{ s}$	Given by the simulation
Run time	$t_{\text{end}} = 220 \text{ s}$	Typical length of the experimental trajectories
Number of runs	$N_{\text{samples}} = 100$	See also figure legends for number of datapoints
Temperature	$T = 300 \text{ K}$	
Standard deviation of MT position	$\sigma_{\text{Pos}} = 30 \text{ nm}$	Measurement uncertainty given by the experiment
Dynein:		
Stiffness within L_0	$k_1 = 0.3 \cdot 10^{-4} \text{ kg/s}^2$	Unknown, estimated by fitting the experimental data of the diffusion coefficient (see figure S3)
Stiffness beyond L_0	$k_2 = 3.0 \cdot 10^{-4} \text{ kg/s}^2$	Reported in [9] for cilia dynein
Stall force	$F_s = 4 \text{ pN}$	Reported in [1] for mammalian cytoplasmic dynein with the adapter protein complex (dynactin+BicD)
Attachment rate	$k_a = 1 \text{ s}^{-1}$	Unknown
Mean forward velocity of individual motors	$v_{f,\text{mean}} = 1200 \text{ nm/s}$	Same order of magnitude as the motility assay of mammalian cytoplasmic dynein (without adapter protein complex) reported in [15]
Backward velocity of individual motors	$v_b = 15 \text{ nm/s}$	Reported in [4] for yeast dynein under high backward load ($F = 10 \text{ pN}$)
Standard deviation of forward velocity distribution	$\sigma_v = 1500 \text{ nm/s}$	Relatively wide velocity distributions were measured in [10, 12] for mammalian cytoplasmic dynein with the adapter protein complex (dynactin +BicD), too.
Left velocity border	$v_{f,\text{lowest}} = 200 \text{ nm/s}$	
Right velocity border	$v_{f,\text{highest}} = 2200 \text{ nm/s}$	

Force free stepping rate of passive attached motors	$s_0 = 85 \text{ s}^{-1}$	Unknown, estimated by fitting the experimental data of the diffusion coefficient (see figure S3), experimental values of [15] were 4 – 5 times higher than the here found exp. values (figure S3), the here found s_0 is also approx. 4 – 5 times higher than the corresponding value of [15]
Activation rate constant	$r_a^0 = 30 \text{ s}^{-1}$	Unknown
Deactivation rate	$r_d = 1 \text{ s}^{-1}$	Unknown
Motor radius	$R^i = 24 \text{ nm}$	Approximated from EM images of mammalian cytoplasmic dynein shown in [15, 12]
kinesin-1:		
Stiffness	$k_2 = 3.0 \cdot 10^{-4} \text{ kg/s}^2$	[6, 5]
Stall force	$F_s = 6 \text{ pN}$	[16]
Detachment force	$F_d = 2.25 \text{ pN}$	[13]
Attachment rate	$k_a = 5 \text{ s}^{-1}$	[7]
Force free detachment rate	$k_d^0 = 1 \text{ s}^{-1}$	[13]
Forward velocity of individual motors	$v_f = 1000 \text{ nm/s}$	[3, 16]
Backward velocity of individual motors	$v_b = 6 \text{ nm/s}$	Same order of magnitude as [2]
Motor radius	$R^i = 4 \text{ nm}$	Same order of magnitude as [14]

Table S1: Simulation parameter values and references. Table of parameters used in the simulation. First column: name or description of the parameter. Second column: symbol and applied value of the parameter. Third column: reference to previous studies and/or explanations about how the value was obtained. In the first part of the table common parameters are given which are similar for dynein and kinesin-1 while in the second and third part dynein and kinesin-1 specific parameters are listed. Note that N_{samples} was 50 for the modified simulations without the activation term and for the number dependencies of the kinesin-1 assay simulation.

References

- [1] Vladislav Belyy, Max A Schlager, Helen Foster, Armando E Reimer, Andrew P Carter, and Ahmet Yildiz. The mammalian dynein-dynactin complex is a strong opponent to kinesin in a tug-of-war competition. *NATURE CELL BIOLOGY*, 18(9):1018–1024, 2016.
- [2] N J Carter and R A Cross. Mechanics of the kinesin step. *Nature*, 435:308–312, 2005.
- [3] David L Coy, Michael Wagenbach, and Jonathon Howard. Kinesin Takes One 8-nm Step for Each ATP That It Hydrolyzes. *THE JOURNAL OF BIOLOGICAL CHEMISTRY*, 274(6):3667–3671, 1999.
- [4] Arne Gennerich, Andrew P Carter, Samara L Reck-Peterson, and Ronald D Vale. Force-Induced Bidirectional Stepping of Cytoplasmic Dynein. *Cell*, 131:952–965, 2007.
- [5] Sylvia Jeney, Ernst H K Stelzer, Helmut Grubmüller, and Ernst-Ludwig Florin. Mechanical Properties of Single Motor Molecules Studied by Three-Dimensional Thermal Force Probing in Optical Tweezers. *ChemPhysChem*, 5:1150–1158, 2004.
- [6] K. Kawaguchi and S. Ishiwata. Nucleotide-dependent single- to double-headed binding of kinesin. *Science*, 291(5504):667–669, 2001.
- [7] C. Leduc, O. Campàs, K.B. Zeldovich, A. Roux, P. Jolimaitre, L. Bourel-Bonnet, B. Goud, J.-F. Joanny, P. Bassereau, and J. Prost. Cooperative extraction of membrane nanotubes by molecular motors. *Proceedings of the National Academy of Sciences of the United States of America*, 101(49):17096–17101, 2004.
- [8] Roop Mallik, Brian C. Carter, Stephanie A. Lex, Stephen J. King, and Steven P. Gross. Cytoplasmic dynein functions as a gear in response to load. *Nature*, 427(6975):649–652, 2004.
- [9] Wallace F. Marshall, editor. *Methods in Enzymology, cilia part 1*. 2013.
- [10] Richard J McKenney, Walter Huynh, Marvin E Tanenbaum, Gira Bhabha, and Ronald D Vale. Activation of cytoplasmic dynein motility by dynactin-cargo adapter complexes. *Science*, 18(345):337–341, 2014.
- [11] M Metropolis, A W Rosenbluth, M N Rosenbluth, A H Teller, and E Teller. Equation of State Calculations by Fast Computing Machines. *J. Chem. Phys.*, 21(6):1087–1092, 1953.
- [12] Max A Schlager, Ha Thi Hoang, Linas Urnavicius, Simon L Bullock, and Andrew P Carter. In vitro reconstitution of a highly processive

- recombinant human dynein complex. *The EMBO Journal*, 33(17):1855–1868, 2014.
- [13] M J Schnitzer, K.Visscher, and S.M.Block. Force production by single kinesin motors. *Nat. Cell. Biol.*, 2(10):718–723, 2000.
- [14] Krzysztof Sozański, Felix Ruhnow, Agnieszka Wiśniewska, Marcin Tabaka, Stefan Diez, and Robert Holyst. Small Crowders Slow Down Kinesin-1 Stepping by Hinder Motor Domain Diffusion. *Phys. Rev. Lett.*, 115(218102):1–5, 2015.
- [15] Takayuki Torisawa, Muneyoshi Ichikawa, Akane Furuta, Kei Saito, Kazuhiro Oiwa, Hiroaki Kojima, Yoko Y Toyoshima, and Ken'ya Furuta. Autoinhibition and cooperative activation mechanisms of cytoplasmic dynein. *Nature Cell Biology*, 16(11), 2014.
- [16] Koen Visscher, Mark J. Schnitzer, and Steven M. Block. Single kinesin molecules studied with a molecular force clamp. *Nature*, 400(6740):184–189, 1999.